Research Article | Vol. 26, No. 8 | 16 Apr 2018 | OPTICS EXPRESS 9389

Optics EXPRESS

Two-dimensional beam-steering device using a doubly periodic Si photonic-crystal waveguide

HIROSHI ABE, MOE TAKEUCHI, GORO TAKEUCHI, HIROYUKI ITO, TOMOKI YOKOKAWA, KEISUKE KONDO, YUYA FURUKADO, AND TOSHIHIKO BABA

Department of Electrical & Computer Engineering, Yokohama National University, 79-5 Tokiwadai, Hodogayaku, Yokohama 240-8501, Japan
**baba-toshihiko-zm@ynu.ac.jp*

Abstract: We demonstrate a nonmechanical, on-chip optical beam-steering device using a photonic-crystal waveguide with a doubly periodic structure that repeats the increase and decrease of the hole diameter. We fabricated the device using a complementary metal–oxide–semiconductor process. We obtained a beam-deflection angle of 24° in the longitudinal direction, while maintaining a divergence angle of 0.3°. Four such waveguides were integrated, and one was selected by a Mach–Zehnder optical switch. We obtained lateral beam steering by placing a cylindrical lens above these waveguides. By combining the lateral and longitudinal beam steering, we were able to scan the collimated beam in two dimensions, with 80 × 4 resolution points.

OCIS codes: (280.3640) Lidar; (230.5298) Photonic crystals.

References and links

1. I. Puente, H. Gonzalez-Jorge, J. Martinez-Sanchez, and P. Arias, "Review of mobile mapping and surveying technologies," Measurement **46**(7), 2127–2145 (2013).
2. T. K. Chan, M. Megens, B. W. Yoo, J. Wyras, C. J. Chang-Hasnain, M. C. Wu, and D. A. Horsley, "Optical beamsteering using an 8 × 8 MEMS phased array with closed-loop interferometric phase control," Opt. Express **21**(3), 2807–2815 (2013).
3. Y. Tang, J. Wang, X. Wang, D. Baofeng, S. Tang, and J. Foshee, "KTN based electro-optic beam scanner," Proc. SPIE **7135**, 713538 (2008).
4. L. Zou, M. Cryan, and M. Klemm, "Phase change material based tunable reflectarray for free-space optical inter/intra chip interconnects," Opt. Express **22**(20), 24142–24148 (2014).
5. J. C. Kastelik, S. Dupont, K. B. Yushkov, V. Y. Molchanov, and J. Gazalet, "Double acousto-optic deflector system for increased scanning range of laser beams," Ultrasonics **80**, 62–65 (2017).
6. S. R. Davis, S. D. Rommel, D. Gann, B. Luey, J. D. Gamble, M. Ziemkiewicz, and M. Anderson, "A lightweight, rugged, solid state laser radar system enabled by non-mechanical electro-optic beam steerers," Proc. SPIE **9832**, 98320K (2016).
7. H. Abediasl and H. Hashemi, "Monolithic optical phased-array transceiver in a standard SOI CMOS process," Opt. Express **23**(5), 6509–6519 (2015).
8. C. V. Poulton, A. Yaacobi, D. B. Cole, M. J. Byrd, M. Raval, D. Vermeulen, and M. R. Watts, "Coherent solid-state LIDAR with silicon photonic optical phased arrays," Opt. Lett. **42**(20), 4091–4094 (2017).
9. J. K. Doylend, M. J. R. Heck, J. T. Bovington, J. D. Peters, L. A. Coldren, and J. E. Bowers, "Two-dimensional free-space beam steering with an optical phased array on silicon-on-insulator," Opt. Express **19**(22), 21595–21604 (2011).
10. K. Kondo, T. Tatebe, S. Hachuda, H. Abe, F. Koyama, and T. Baba, "Fan-beam steering device using a photonic crystal slow-light waveguide with surface diffraction grating," Opt. Lett. **42**(23), 4990–4993 (2017).
11. X. Gu, T. Shimada, A. Matsutani, and F. Koyama, "Miniature nonmechanical beam deflector based on Bragg reflector waveguide with a number of resolution points larger than 1000," IEEE Photonics J. **4**(5), 1712–1719 (2012).
12. T. DiLazaro and G. Nehmetallah, "Multi-terahertz frequency sweeps for high-resolution, frequency-modulated continuous wave ladar using a distributed feedback laser array," Opt. Express **25**(3), 2327–2340 (2017).
13. T. Baba, A. Motegi, T. Iwai, N. Fukaya, Y. Watanabe, and A. Sakai, Light propagation characteristics of straight single-line-defect waveguides in photonic crystal slabs fabricated into a silicon-on-insulator substrate," IEEE J. Quantum Electron. **38**(7), 743–752 (2002).
14. G. Roelkens, D. V. Thourhout, and R. Baets, "High efficiency grating coupler between silicon-on-insulator waveguides and perfectly vertical optical fibers," Opt. Lett. **32**(11), 1495–1497 (2007).

#319814 https://doi.org/10.1364/OE.26.009389
Journal © 2018 Received 16 Jan 2018; revised 2 Mar 2018; accepted 26 Mar 2018; published 2 Apr 2018

Optics EXPRESS

15. Y. Terada, K. Miyasaka, K. Kondo, N. Ishikura, T. Tamura, and T. Baba, "Optimized optical coupling to silica-clad photonic crystal waveguides," Opt. Lett. **42**(22), 4695–4698 (2017).

1. Introduction

Compact light detection and ranging (LiDAR) devices can be used to measure and image the distances to surrounding objects for automatic driving, control of robots and drones, three-dimensional (3D) mapping, and so on. For close objects, compound-eye cameras based on parallax and flash LiDARs that emit light pulses in all directions and perform ranging using high-speed cameras will be competing technologies. LiDARs with the capability for two-dimensional (2D) beam steering using optical deflectors are advantageous for distances greater than several tens of meters and/or outdoors under sunlight, when the parallax and returned-light intensity decrease. Conventional optical deflectors are mechanical devices that use the rotation of the device itself or a deflecting mirror, and they have problems such as large size, high cost of assembly, and instability to vibrations of the moving body [1]. Microelectromechanical systems (MEMS) [2], electro-optic effects [3], phase-change materials [4], acousto-optic effects [5], and liquid crystals [6] have also been studied, but their small deflection angles, large beam divergence, and/or slow response speeds are still problems. Recently, the development of nonmechanical optical deflectors fabricated using silicon (Si) photonics technology has become an active area of study. The two major structures of this type are optical phased arrays [7, 8], which adjust the optical phase to form an arbitrary light beam, and waveguide gratings [8, 9], which change the diffraction angle of the guided mode, depending on the wavelength and the refractive index of the waveguide. However, to form a sharp beam with a phased array requires a large number of optical antennas and fine phase adjustment of each antenna, which is extremely complicated. For waveguide gratings, beam formation is easier, but the deflection angles are small. For optical deflectors, the number of resolution points—given by $N_\theta \equiv \Delta\theta/\delta\theta$, where $\Delta\theta$ is the deflection angle and $\delta\theta$ is the beam divergence—is especially important. Assuming that N corresponds to the number of pixels in a given direction, more than a hundred points are needed for a deflector to be practical to use with a LiDAR.

We have recently reported a photonic-crystal waveguide (PCW)—fabricated using a Si-photonics complementary metal–oxide–semiconductor (CMOS) process—that is coupled to a surface grating [10]. This device guides a slow-light mode, radiates it into free space to form a fan-shaped beam, and acts like a nonmechanical deflector that achieves a large $\Delta\theta$. In a similar study, a deflector using the large angular dispersion of a leaky, multilayer waveguide has also been reported [11]. In our previous study, we used the PCW to facilitate dispersion control and ensure compatibility with the CMOS process, which allows the integration of various additional components. We obtained beam deflection in the direction along the waveguide (the longitudinal direction or θ-direction), with $\Delta\theta = 23°$, $\delta\theta = 0.23°$, and $N = 100$ for a wavelength sweep of $\Delta\lambda = 27$ nm. Such a device is usable as a beam scanner in the above applications including LiDARs in combination with a swept laser module [12] and/or by adding some index control mechanism into the PCW such as heaters for the thermo-optic effect.

In the present paper, on the other hand, we report a device, shown in Fig. 1(a), that more easily achieves the same function as a surface grating by introducing a doubly periodic pattern in the PCW. Furthermore, we report the creation of a point beam formed by loading a cylindrical lens, with deflections in the direction orthogonal to the waveguide (the lateral direction or ϕ-direction) obtained by exploiting multiple deflectors, and we have successfully demonstrated 2D deflection.

Optics EXPRESS

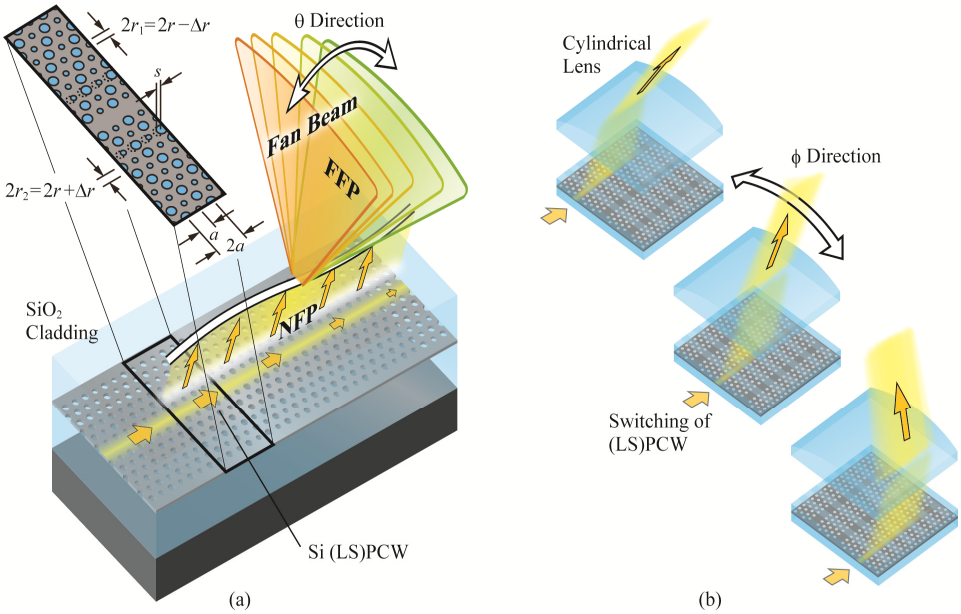

Fig. 1. Schematic illustration of a Si (LS)PCW beam-steering device with a doubly periodic structure. (a) Single (LS)PCW for beam steering in the θ-direction. (b) Multiple (LS)PCWs for beam steering in the ϕ-direction. The abbreviations NFP and FFP denote the "near-field pattern" and "far-field pattern," respectively. See text for additional details.

2. Structure and theoretical performance

Si PCWs consist of circular holes arranged in a triangular lattice in a Si slab encased in SiO_2 cladding, sandwiching a line-defect waveguide core. The structural parameters for operation at telecom wavelengths are the Si slab thickness t = 210 nm, the circular hole diameter $2r$ = 215 nm, and the lattice constant a = 400 nm. A slow-light mode is guided along this waveguide, which has a large group index n_g = 10–80. In a lattice-shift-type PCW (LSPCW) that we have developed, low-dispersion slow light occurs with an almost constant n_g over a specific wavelength band Δλ. In a typical structure of this kind, the third rows of holes from the waveguide are longitudinally shifted by s = 90 nm. When a double periodicity Λ = $2a$ is introduced along the waveguide in such a structure, light is radiated diagonally upward and downward. In [10], a grating was formed on the surface of the upper SiO_2 cladding, whereas in the present study, $2r$ was increased or decreased by ± Δr with period Λ along the waveguide; i.e., $2r_1 = 2r + \Delta r$, $2r_2 = 2r-\Delta r$, and $2r_{av} = r_1 + r_2$.

For the surface grating type structure, we first fabricate the LSPCW with a flattened SiO_2 cladding using CMOS process and then perform the post process of thinning the cladding and forming the surface grating. The light radiation is particularly sensitive to the distance between the Si slab and grating; the thinning process requires 10-nm order accuracy. Although the surface grating may be fabricated in the CMOS process, such accuracy is still a technical challenge. On the other hand, in the doubly-periodic structure of this study, such complicated process is not needed, and the structure can be fabricated with sufficient accuracy in the CMOS process, which is a significant advantage. For the doubly periodic modulation, various patterns can be considered. In this study, we arranged it in a V shape, as shown in Fig. 1. For this pattern, we calculated a single-lobed profile of radiated beam, as shown below.

Assuming that the direction perpendicular to the Si slab is 0°, θ is given by [10]

Optics EXPRESS

$$\theta = \sin\left(\frac{\beta}{k_0} - \frac{\lambda}{2a}\right), \tag{1}$$

where β and k_0 are the propagation constant of the slow-light mode and the wave number in vacuum, respectively, and λ is the wavelength. The quantity of β is obtained from photonic band calculations using a 3D model with the above parameters, as shown in Fig. 2(a). The slow-light mode lies in the range between the band edge on the long-wavelength side (the Bragg condition) and the SiO_2 light line on the short-wavelength side (the total reflection condition at the Si/SiO_2 boundary). Figure 2(b) shows the group index spectrum, where $n_g = c(d\beta_0/d\omega) = -(\lambda^2/2\pi)(d\beta_0/d\lambda)$, and ω is the angular frequency. By introducing the lattice shift s, low-dispersion slow light is obtained for $n_g \approx 20$ and $\Delta\lambda \approx 15$ nm (λ = 1550–1565 nm). Including both ends of the transmission band, where n_g decreases or increases markedly, light can propagate in the bandwidth Δλ = 27 nm (λ = 1550–1577 nm). Reflecting this result, we obtain θ, as shown in Fig. 2(c). When λ is changed within the above range, θ varies over the range 0–27° (Δθ = 27°), and the average sensitivity is $d\theta/d\lambda = 1°/\text{nm}$. This value is as large as 7 times that of a normal Si waveguide grating, reflecting the fact that the angular dispersion is proportional to n_g [10].

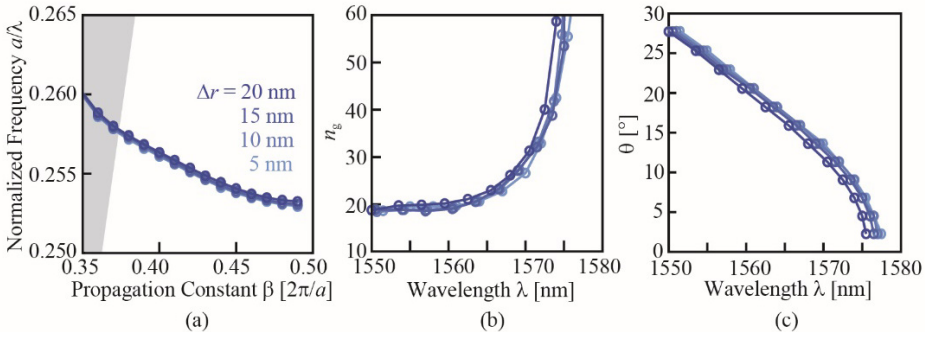

Fig. 2. Theoretical characteristics of a doubly periodic LSPCW. (a) Photonic band. The gray zone depicts the SiO_2 light cone. (b) Group index spectrum. (c) Radiation angle.

Note that even when the doubly periodic modulation of the hole diameter is changed over the range Δr = 5–20 nm in the above calculations, the changes in the photonic band and θ are small. This is because the hole diameter is increased or decreased around $2r_{av}$ so as not to change the band. On the other hand, as shown in Fig. 3(a), the light-radiation coefficient α_{rad} changes greatly, depending on the value of Δr. Here $\alpha_{rad} = n_g/c\Delta\tau$ is obtained from the time constant Δτ at each wavelength when a slow-light pulse is excited, from the 3D finite-difference time-domain calculation with the periodic boundary condition [13]. With changes in Δr, the value of α_{rad} at the central wavelength changes greatly, from 30 dB/cm to 800 dB/cm. Because the propagation condition for slow light is not satisfied at wavelengths shorter than the light line, α_{rad} becomes larger than 1000 dB/cm, which is unusable. Also, α_{rad} becomes several times larger near the band edge, due to the increase of n_g. When α_{rad} is constant over the LSPCW, the radiation decays exponentially during propagation, due to the attenuation of the slow-light mode caused by the radiation itself and original waveguide loss α_{loss}. When the length L of the LSPCW is sufficiently long, the exponential decay is Fourier-transformed into a Lorentzian far-field pattern (FFP), and its beam divergence δθ, defined as the full width at half maximum, is calculated, as shown in Fig. 3(b). When $\alpha_{rad} + \alpha_{loss} \le 100$ dB/cm (or ≤50 dB/cm), δθ is ≤0.04° (or ≤0.03°) for L = 3 mm, respectively. In the latter case, $N_\theta > 900$ resolution points are available. When $\alpha_{rad} + \alpha_{loss}$ = 100–150 dB/cm and L = 1 mm, which is the case for the experiment described later, δθ will be a value around 0.1°. The insertion loss from the input end of the LSPCW to the radiation in free space, *Loss*, occurs

Optics EXPRESS

due to the original waveguide loss α_{loss} and residual components passing through the LSPCW without radiation. It is given by

$$Loss\,[\mathrm{dB}] = -10\log_{10}\int_0^L \zeta\alpha_{rad}\exp[-(\alpha_{rad}+\alpha_{loss})z]dz \ , \qquad (2)$$

where ζ is the ratio of useful radiation for the optical beam to all the incident power. If the waveguide structure is symmetric in the vertical direction, the radiation occurs equally in the upper and lower directions. In addition, the light extraction may partly be hampered by the reflection at the boundary between the SiO_2 cladding and air. Therefore, ζ is considered to be less than 0.5 for the upper radiation in the present device. However, this ratio will be increased close to one by employing some asymmetric structure similar to that of the grating couplers in Si photonics [14]. To focus on the optimization of α_{rad}, we assumed $\zeta = 1$ here and estimated the *Loss*, as also shown in Fig. 3(b). We assumed α_{loss} = 10–30 dB/cm as typical values for n_g ≈ 20 of slow light. A small α_{rad} achieves a small $\delta\theta$ while increasing the *Loss* because the influence from α_{loss} and residual components is relatively increased. A small $\delta\theta$ and low *Loss* of ≤ 1 dB is well-balanced when L = 1–3 mm and $\alpha_{rad} + \alpha_{loss}$ = 100–150 dB/cm.

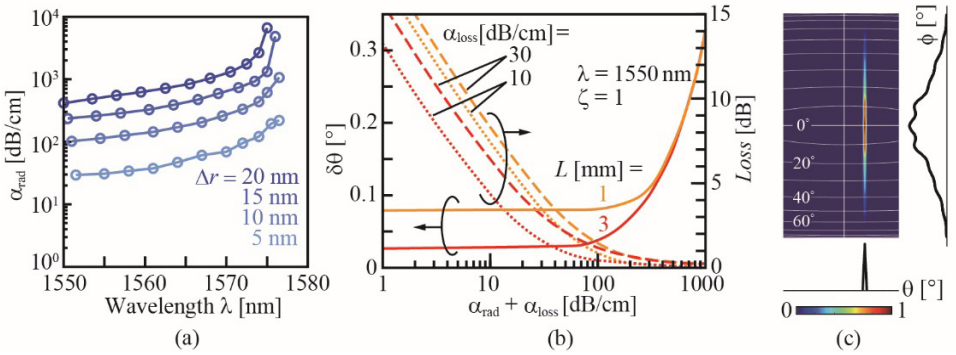

Fig. 3. Calculation of (a) radiation coefficient α_{rad}, (b) beam divergence $\delta\theta$ (solid lines) and insertion loss (dotted and dashed lines) and (c) fan beam profile projected on the θ-ϕ plane. For the estimation of loss in (b), the downward radiation and internal reflection are neglected. For (c), a vertically symmetric structural model, neglecting the bottom substrate, and θ = 2.2° are assumed. The weak oscillation in the ϕ profile originates not from the device structure but from unwanted reflection at boundaries of calculation model.

In the lateral direction, on the other hand, the slow-light mode, which is strongly confined within the LSPCW, is radiated and spreads widely in free space, so the radiation beam becomes fan-shaped. An example of calculated beam profile is shown in Fig. 3(c). To collimate this beam, we loaded the LSPCW with a cylindrical lens, like that shown in Fig. 1(b). Furthermore, if multiple PCWs are integrated, and a PCW to which incident light is coupled can be selected, the deflection angle ϕ in the lateral direction varies depending on the relative positional relationship between the selected PCW and the lens. The value of ϕ for light originating from an LSPCW at a lateral distance W from the optical axis of the lens is given by $\phi = \tan^{-1}(W/f)$, where f is the focal length of the lens. For example, ϕ = 1.9° for W = 100 μm and f = 3 mm.

3. Experiment

We fabricated the device used in this investigation using a CMOS process that exploits KrF excimer laser exposure, and we used a phase-shift mask to obtain a resolution of less than 130 nm. The substrate was a 200-mm silicon-on-insulator chip with a Si layer 210 nm thick and an SiO_2 BOX layer 2 μm thick. Figure 4(a) shows the fabricated PCW with the V-shaped doubly periodic modulation in hole diameter. The structural details were the same as those described in the calculation. The length L was 1 mm, and the input end was connected to a Si

Optics EXPRESS

wire waveguide via an optimized tapered structure [15]. Continuous-wave transverse-electric-polarized light from a tunable laser source was coupled to the wire waveguide through a spot-size converter and was directed onto the PCW. We first evaluated the propagation loss of the PCW without double periodicity ($\Delta r = 0$) to be $\alpha_{loss} \approx 30$ dB/cm by measuring the light output for several samples with different L. Then, we obtained the near field pattern (NFP) of light propagation using a microscope (Synergy Optosystems, M-Scope type S) with × 50 objective lens and InGaAs camera (Hamamatsu Photonics C14041-10U) whose pixel pitch is 20 μm and its intensity profile for the device of Δr = 10 nm, as shown in Fig. 4(b). The intensity decays almost exponentially and its linear fitting gives $\alpha_{rad} + \alpha_{loss} \approx 150$ dB/cm, meaning $\alpha_{rad} \approx 120$ dB/cm, which agrees with the calculation in Fig. 3(a). It satisfies the optimum condition that balances the small beam divergence δθ and low insertion loss. We also observed the FFP of the light radiated from the PCW using another microscope (Synergy Optosystems, M-Scope type F) with × 10 objective and the same type of InGaAs camera. The angular resolution of this setup was 0.14°. The microscope was fixed on a rotation stage so that we could observe the wide range of θ in the range of 0–35°. An example FFP is shown in Fig. 4(b). As mentioned above, we observed the FFP to be a fan-shaped beam that was thin in the θ-direction and wide in the ϕ-direction. Although the observable angular range by the used microscope and camera could cover the full range of the calculated beam profile, it appears to be similar to that in Fig. 3(c) except for the slight curvature of the fan beam caused by the aberration of the used microscope. Figure 4(c) shows the overlay of FFPs at different λ values, separated by 1 nm spacings, and Fig. 4(d) summarizes the θ-versus-λ characteristics; obviously, θ changed depending on λ. The operating band was shifted by changing $2r$. The slope of the θ-versus-λ curve increased as $2r$ increased, reaching a maximum value of ~1°/nm for $2r$ = 230 nm. This agrees well with the calculated value. The deflection angle Δθ = 24° is slightly smaller than the calculated value, which is due to the abrupt increase in both n_g and the radiation loss, as well as to suppressed radiation near θ = 0°, corresponding to the Bragg condition at the band edge. Figure 4(e) shows the beam divergence δθ, defined as the full width at half maximum. It decreased toward shorter wavelengths, reaching a minimum value of 0.2°, whereas it increased toward longer wavelengths, particularly near the band edge. The average value over the wavelength range was 0.3°, which gives $N_\theta = 80$. However, because this value is affected by the resolution limit of 0.14° for the setup and camera used, δθ is actually somewhat smaller, similar to that in [10], so we may be able to expect $N_\theta > 100$.

In the used setup, it was difficult to directly measure the output power. So, we evaluated the total loss from the laser source to the radiation by summing each loss, which was measured in other experiments or calculated, as follows: 1 dB in a lens module of the input fiber (measured), 1.8 dB from the module to the spotsize converter of the device chip (measured), < 0.1 dB in the Si wire waveguide (measured), 0.4 dB at the junction between the Si wire and PCW (measured), ~1 dB in the radiation from the doubly-periodic LSPCW (calculated in Fig. 3(b)) and 3–4 dB due to the existence of the downward radiation and reflection at the boundary between the top SiO_2 cladding and air (calculated). Therefore, the total loss from laser source to the radiation was ~8 dB in the present device. The loss of the lens module can be eliminated by using a lensed fiber. The minimum loss of the PCW, α_{loss}, we have measured is 8 dB/cm, and then the loss in the radiation process will be < 0.5 dB. We also expect to reduce the sum of the downward radiation and internal reflection to <1 dB by employing an asymmetric structure of the PCW, as mentioned above. Therefore, the total loss will be < 4 dB in the near future.

Optics EXPRESS

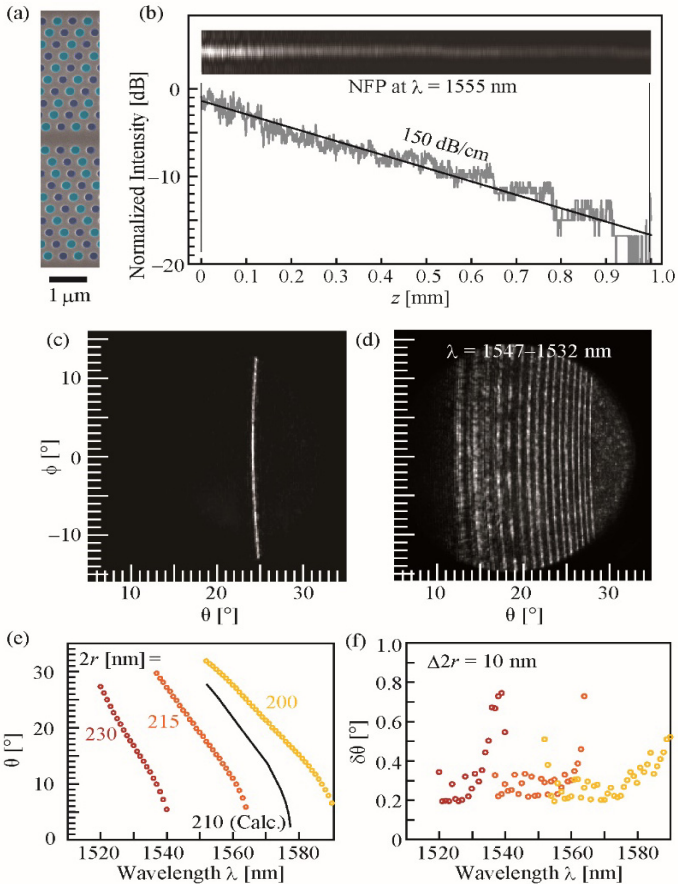

Fig. 4. Fabricated device of Δr = 10 nm and its 1D beam steering characteristics. (a) Scanning electron micrograph of the fabricated device. The large and small holes are light-blue and dark-blue colored, respectively. (b) Observed NFP of the light propagation and its decay along the waveguide. The NFP is 10 times expanded in the lateral direction. The gray line is row data of the intensity profile and black line is the linear fitting. (c) Observed FFP of the fan beam. (d) θ beam steering for each 1 nm change in λ. (e) Beam angle; the black line shows the calculated values. (f) Beam divergence.

To reshape the fan beam into a point beam and deflect it in the ϕ-direction, four PCWs were arrayed with a 100 μm pitch (Fig. 5(a)), one was selected by three 1 × 2, heater-controlled, Mach–Zehnder-type switch (Fig. 5(b), and a 5-mm-diameter rod lens with f = 3.8 mm was loaded above the chip (Fig. 5(c)). The rod lens was aligned parallel to the PCWs so that the radiated fan beam is collimated in the ϕ direction. The fan-shaped beam was collimated into a point beam, as shown in Fig. 5(d). (Only a few pixels of the camera detected light because of its resolution limit.) Figs. 5(e) and 5(f) show the NFPs and FFPs when the PCW was switched between the four LSPCWs, and light was radiated in a fan beam with Δϕ = 1.5–1.8° in each case. Assuming the pitch between the PCWs to be equal to W, we calculated Δϕ to be 1.5° from the above equation, which agrees roughly with the experimental result. The beam divergence in the ϕ direction, δϕ, is approximately 0.3°, which is five-times smaller than Δϕ. Therefore, the number of resolution points in the ϕ direction, N_ϕ, can be increased simply by enlarging the size and focal length of the lens; employing a 25-mm-diameter rod lens makes the situation Δϕ ≈δϕ and achieves the dense beam scanning with five-times larger N_ϕ. When the size of the lens is fixed and the number of PCWs is increased, N_ϕ is further increased but the aberration of the lens expands δϕ and limit the maximum N_ϕ,

Optics EXPRESS

which should be an important issue to be investigated and improved. However, if this device is applied to LiDARs in vehicles, $N_\phi << N_\theta$ may be acceptable, because the lateral resolution is more important than the vertical resolution for identifying, for example, man and cars, and we will be able to apply N_θ and N_ϕ to sensing the lateral and vertical profiles of objects by orienting the device appropriately.

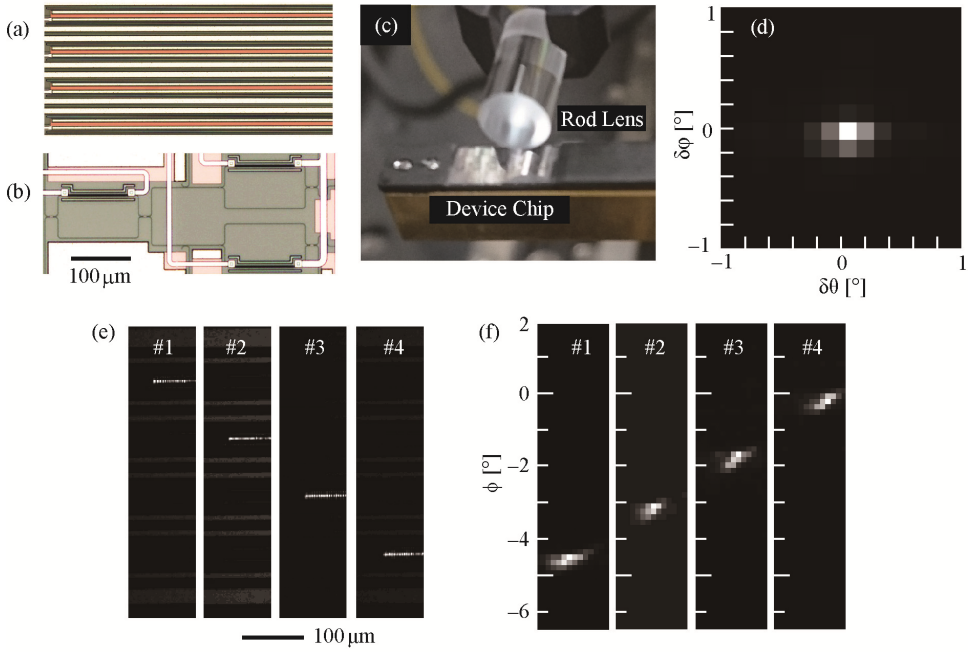

Fig. 5. Beam-steering characteristics of the fabricated device in the ϕ-direction, which was observed by the same setup as for Fig. 4. (a) LSPCW array. (b) Three 1 × 2, heater-controlled, Mach–Zehnder optical switch. (c) Appearance of the device chip and rod lens. (d) Profile of the point beam. (e) NFP of light propagating in the four LSPCWs #1–#4. (f) FFP of ϕ-directional beam steering.

By combining θ control via the λ sweep and ϕ control via switching of the LSPCWs, 2D beam steering becomes possible. Figure 6(a) shows the variation of the beam-collimation characteristics of the rod lens used for θ control. The distance to the rod lens was adjusted so that the beam was correctly collimated at θ = 15°. However, when θ changes, both the distance from the PCW to the lens and the focal length of the lens change, and beam divergence δϕ occurs. Figure 6(b) summarizes the resulting values of δϕ, defined as the full width at half maximum. When the distance to the lens was adjusted so that δϕ reached a minimum value of less than 0.2°, the maximum value of δϕ was 0.97°. Because this value is smaller than the deflection angle Δϕ, the number of resolution points is not affected by this defocusing. Beam divergence can also be reduced by optimum design of the lens. Figure 6(b) shows the FFP when the beam was swept in 2D while the point beam was formed by adjusting the distance to the lens for every θ. The point beam was moved continuously in the θ-direction by the λ sweep and discretely in the ϕ-direction by the optical switch. Although the spot shown here provides a 2D resolution of 45 × 4, $N > 80 \times 4$ is possible, considering the measured resolution points in the θ-direction. The deflection angle Δϕ can be reduced by reducing the PCW pitch W and/or by using a lens with a larger f. By improving the resolution of the measurement setup and increasing the number of PCWs, it is easy to increase N by more than a factor of 10 beyond that achieved in these experiments.

Optics EXPRESS

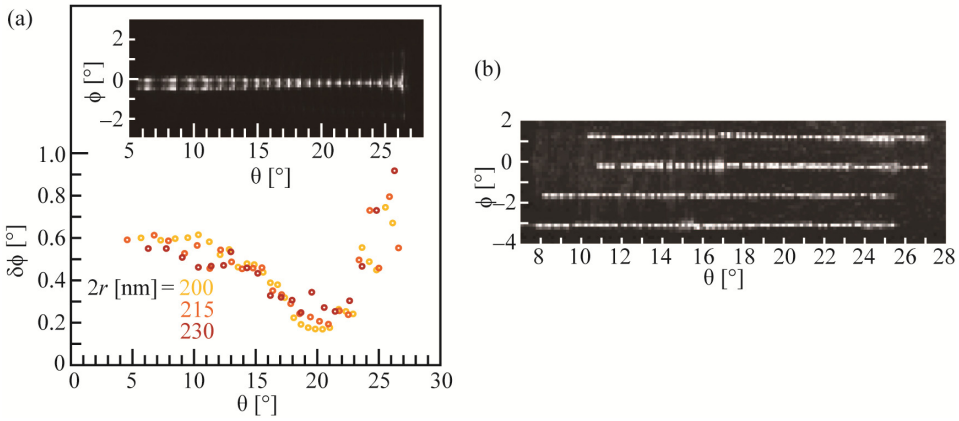

Fig. 6. 2D beam steering. (a) Lateral beam divergence of the point beam with θ-directional steering. The inset shows the FFP. (b) 2D beam steering by λ scanning and LSPCW switching, where the position of the rod lens was adjusted for each θ.

4. Conclusion

We have succeeded in operating a collimation-lens-loaded Si PCW with doubly periodic hole diameters as a 2D optical deflector. The radiation beam angle is controlled in the longitudinal and lateral directions, respectively, by sweeping the wavelength and by switching the waveguides. We fabricated the device using a CMOS process, and we observed the formation of a point beam, which we were able to steer in 2D. The number of resolution points was 80 or more in the longitudinal direction and four in the lateral direction. The resolution can be further increased by more than a factor of 10 by improving the measurement setup and increasing the number of PCWs.

Funding

This study was supported by Accelerated Innovation Research Initiative Turning Top Science and Ideas into High-Impact Values (ACCEL); Japan Science and Technology Agency (JST) (JPMJAC1603).